JGR Planets

Key Points:

- Shortening landforms on Mars were analyzed at the surface and subsurface to quantify their morphometrics and structural geometries
- Traditional definitions of lobate scarps and wrinkle ridges are end member descriptions of landforms that exist across a morphological spectrum
- Lobate scarps are fault-dominated structures while wrinkle ridges are fold-dominated structures

Correspondence to:

K. T. Crane,
ktcrane@seres-es.com

Author Contributions:

Conceptualization: Leta R. McCullough, Kelsey T. Crane, Christian Klimczak
Data curation: Leta R. McCullough, Kelsey T. Crane, Christian Klimczak
Formal analysis: Leta R. McCullough, Kelsey T. Crane, Christian Klimczak
Funding acquisition: Kelsey T. Crane, Christian Klimczak
Investigation: Leta R. McCullough, Kelsey T. Crane, Christian Klimczak
Methodology: Leta R. McCullough, Kelsey T. Crane, Christian Klimczak
Project administration: Kelsey T. Crane, Christian Klimczak
Resources: Kelsey T. Crane, Christian Klimczak
Software: Leta R. McCullough, Kelsey T. Crane
Supervision: Kelsey T. Crane, Christian Klimczak
Validation: Leta R. McCullough, Kelsey T. Crane

Morphological and Structural Characterization of Shortening Landforms on Mars

Leta R. McCullough[1] , Kelsey T. Crane[2] , Stephan R. Loveless[3] , and Christian Klimczak[3]

[1]Department of Geosciences, Planetary Structural Geology and Tectonics Group, Mississippi State University, Mississippi State, MS, USA, [2]Seres Engineering & Services, LLC, Charleston, SC, USA, [3]Geology Department, Center for Planetary Tectonics, University of Georgia, Athens, GA, USA

Abstract The lithosphere of Mars accommodates horizontal shortening through folding and faulting, producing landforms described as wrinkle ridges or lobate scarps. Despite this nomenclature, we lack a deep understanding of the drivers of morphological differences observed between landform types. This study aims to develop a quantitative model for shortening landform classification based on surface morphology, subsurface architecture, and strain accommodation, facilitating interpretations of where and how lithospheric stresses are recorded. We developed this model by mapping 100 shortening landforms in a Geographic Information System, recording 12 unique geomorphic parameters such as length and asymmetry, and estimating the strain of each landform. We conducted a Discriminant Function Analysis (DFA) using surface morphometrics. This DFA produced a predictive linear function for categorizing wrinkle ridges and lobate scarps and for quantifying which landforms were exemplars within those categories. The three most influential variables on the surface morphometry DFA were the maximum width, forelimb slope, and back limb length. We then modeled the subsurface structural geology of 50 landforms using MOVE Structural Geology Modeling Software and conducted a second DFA based on subsurface metrics. DFA was most influenced by the dip and depth of the lower ramp base. When both surface morphology and subsurface geometry are input into single DFA, wrinkle ridges and lobate scarps can be distinguished quantitatively 96% of the time. Our results also show that lobate scarps accommodate more strain and imply that studies should consider landform type when interpreting local, regional, and global geological stress histories.

Plain Language Summary The tectonic structures of a planet record its geologic history. Some of these structures, such as those classified as lobate scarps and wrinkle ridges, account for the horizontal shortening of the planet's surface. These two groups of shortening structures are observed on the surface of almost every rocky planet. Planetary geologists have historically assumed that wrinkle ridges and lobate scarps represent different types or amounts of shortening based on differences in their visual morphologies. In this work, we mapped 100 of these landforms on Mars and quantified their surface characteristics. We then further analyzed 50 landforms using a structural geology modeling software to assess their subsurface fault and fold geometries. Using the parameters we measured, we applied a statistical analysis called a Discriminant Function Analysis to quantify and learn about the differences between these landform types. We find that lobate scarps are rooted by faults that extend deeper into the subsurface than faults that underly wrinkle ridges, and that because of the greater variability in landform characteristics, lobate scarps may represent a range of stages in the formation of these landforms while wrinkle ridges developed entirely during one phase of the geologic history of Mars.

1. Introduction and Motivation

Shortening landforms have been observed on all rocky bodies, including planets hosting a singular tectonic plate that constitutes their lithospheric lid, such as Mars or the Moon (Breuer & Spohn, 2003; Nimmo & Stevenson, 2000; Strom et al., 1975; Watters, 1992). These landforms develop when horizontally compressive stresses reach the strength of the lithosphere, resulting in shortening expressed by thrust faulting and folding. On Earth, we typically associate shortening as the result of contractional plate tectonic phenomena such as convergent plate motions and mountain building (Ramsay, 1969). However, on Mars or other single-plated planetary bodies, we must intentionally broaden our perspectives of shortening origins. Shortening landforms on one-plate planets can be formed by stresses from long, sustained planetary cooling, stresses resulting from cratering and basin tectonics, volcanic processes, mantle convection, mass loading, etc (Mueller & Golombek, 2004). Contractional tectonic

environments on single-plated lithospheres may be sustained through local, regional, or global processes. Furthermore, with little to no erosion on these bodies, the true shapes of shortening landforms can be preserved for geologically long time scales such that the present morphometrics of these landforms can be completely attributed to the tectonic processes that caused them (Klimczak et al., 2018).

Many processes result in unique populations of shortening landforms. Contraction due to planetary cooling has been demonstrated to result in a global population of randomly oriented shortening structures on the Moon and Mercury (Nahm & Schultz, 2011; Ruj & Kawai, 2021; Watters, T.R., 2021; Yue, Z et al., 2017). Many studies have inferred that these landforms may be underlain by thrust faults which cut deeply into the lithosphere to allow for global-scale lithospheric shortening (Andrews-Hanna, 2020; Egea-Gonzalez et al., 2012; Herrero-Gil et al., 2019; Klimczak et al., 2018; Nimmo & Watters, 2004). In contrast, volcanism and associated loading due to the addition of volcanic materials to a planet's surface result in more localized stratigraphically controlled deformation (Comer et al., 1985; Golombek & Phillips, 2010; Tenzer et al., 2015), which can be described as thin-skinned tectonics (e.g., Crane, 2020). Shortening landforms have been observed tangential to these added masses, whether they be near volcanic edifices (Byrne et al., 2012; Tanaka et al., 1991) or effusive deposits (Leverington & Maxwell, 2004; Schultz, 1976). One may infer that localized landforms are associated with shallower thrusts, rooting into layers associated with the addition of volcanic materials (e.g., Crane, 2020). The spatial distribution and orientation of the shortening landforms inform our understanding of the orientation and spatial patterns of strain, but not the amount of or mechanism by which lithospheric shortening is accommodated on individual structures. Crucially, to understand the magnitude of strains associated with these processes, we must develop a deeper understanding of shortening landforms and the strain they represent.

Many studies postulate that different landforms represent different styles of deformation (e.g., Karagoz et al., 2022; Mueller & Golombek, 2004; Watters, 1993; Zuber et al., 2010), but currently there is no quantitative way to categorize shortening landforms. Categorization, however, should be rigorously tested as distinctive morphologies could imply unique kinematic and dynamic structural development. On Mercury, Mars and the Moon, landforms have been qualitatively sorted into three categories: lobate scarps, wrinkle ridges, and high relief ridges (Watters, 1992), with a small minority of shortening landforms being described as the latter, based on visual and topographic inspection. Focused on the landforms of Mars, our research goal is to conduct a statistical investigation to quantitatively describe the differences between lobate scarps and wrinkle ridges so that they can be uniquely interpreted. This model lays the groundwork for future investigations of crustal properties, geological histories, and stress magnitudes associated with various processes in which landform interpretation is key.

1.1. Lobate Scarps and Wrinkle Ridges: Our Current Understanding

Lithospheric shortening causes positive relief landforms that are often asymmetric in profile and include a steep front scarp paired with a gentler sloping back limb. Although both lobate scarps and wrinkle ridges fit this general description, their surface morphologies, map patterns, and visible structures differ widely, and in some locations, the two landform groups coexist across a gradient (e.g., Atkins et al., 2022). On Mars, lithospheric and lithologic differences across the hemispheric dichotomy boundary may accentuate these differences (Khan et al., 2021; Phillips, 1992; Rich, 2023).

Wrinkle ridges are observed to have broad asymmetric to symmetric profiles, with secondary smaller wavelength topographic peaks superimposed across their profiles (Figures 1a and 1b; Watters & Nimmo, 2010). The direction of asymmetry may vary along the landform length. This is also referred to as a change in vergence or direction of tectonic transport and results from a change in the dip direction of the underlying fault (Crane & Klimczak, 2019b; Okubo & Schultz, 2003; Watters, 2004). On Mars, wrinkle ridges are reported to range from tens to hundreds of km long, have 80–250 m of relief, and are 10–20 km in width (Korteniemi et al., 2015). Wrinkle ridges may have linear to arcuate planforms, and on Mars, the planform morphology is often fragmented into separate rises along-strike offsets (Golombek et al., 2001). Concentric wrinkle ridges surround the shield volcanoes on the Tharsis magmatic complex in the western hemisphere (Karagoz et al., 2022; Okubo & Schultz, 2004; Watters & Nimmo, 2010), while concentric map patterns are also observed encircling volcanically flooded impact craters (Klimczak et al., 2012). Wrinkle ridges in close vicinity to one another are also observed in plains settings such as the Lunae Planum and Solis Planum, where ridges are roughly parallel and evenly spaced (Golombek et al., 2001; Plescia, 1991; Watters, 1991).
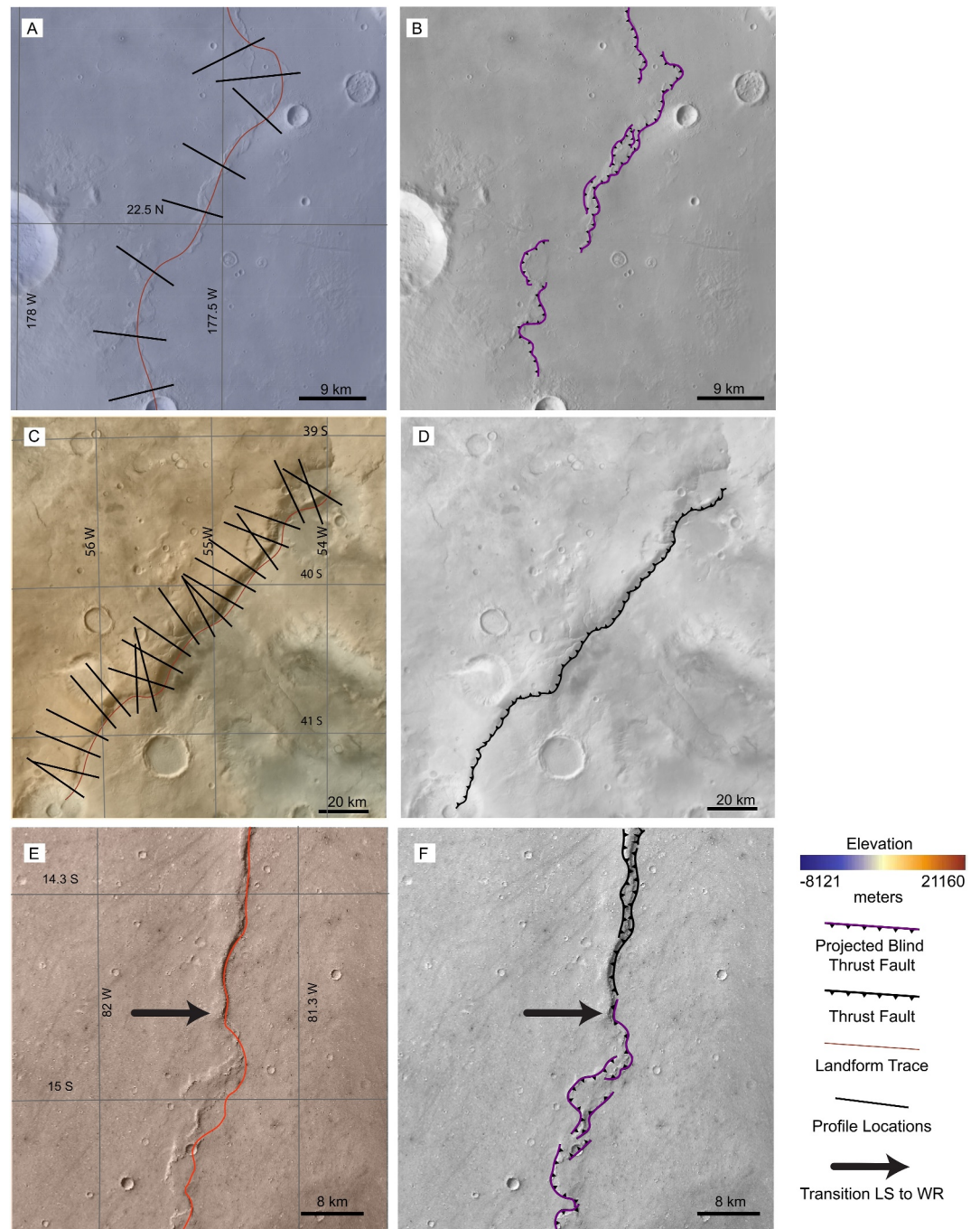
Figure 1. Images of a wrinkle ridge (panels a and b), a lobate scarp (c, d), and a landform transitioning structure between the two classification types along its length (e, f). In panels (a, c, and e). Images are from the Context Camera mosaic and left column images are additionally overlayed by colorized Mars Orbiter Laser Altimeter topography data (Bell et al., 2013; Fergason et al., 2018; Malin et al., 2007). Red lines indicate the rough planform pattern of the landform, and black lines show where topographic profiles were collected across the landforms. Each image is projected in Orthographic projection centered on the landform mid-point (40°S, 55°W; 22.5°N, 177.5°W; 14.3°S, 81.3°W). In panels (b, d, and f), the same landforms are shown with mapped fault traces with teeth on the fault hanging walls.

Complex surface morphologies of Martian shortening landforms pose a very interesting question about their subsurface architecture: is it just as complicated or is it simpler? Because thrusts are not described as surface-breaking along the steep face of the landforms, wrinkle ridges are commonly interpreted as being underlain by

one or more blind (entirely subsurface) thrust fault(s) (Mueller & Golombek, 2004; Okubo & Schultz, 2004). The blind nature of this fault, combined with interpreted fracturing and extensive folding, has made more precise interpretations of subsurface structure and strain estimations particularly challenging. However, studies of small subsurface exposures and several proposed Earth analogs to these features have allowed for some ground-truthing and have improved our current understanding of their subsurface fault geometries (Cole & Andrews-Hanna, 2017; Crane & Klimczak, 2019a; Golombek et al., 1991). There are many cases where models have emphasized the importance of folding (Crane, 2020; Herrero-Gil et al., 2020). However, these models have yet to consider the case of propagating faults through mechanically weak layers, which on Mars is evidenced by irregular surface topography, (Crane, 2020; Schultz, 2000), back and secondary thrusts (Andrews-Hanna, 2020; Cole & Andrews-Hanna, 2017), and the presence of weak deep layers from which faults propagate upward into stronger layers (Kreslavsky & Basilevsky, 1998). Weak layers are hypothesized to originate from salt deposition (Andrews-Hanna, 2009; Montgomery et al., 2009), ice-rich units (Mangold et al., 1998), impact cratering-generated regolith layers (Crane & Klimczak, 2019b), contacts between strong and weak layers (Okubo & Schultz, 2004), or as contacts between volcanic units (as on Earth; Gudmundsson & Brenner, 2004). Generally, the average subsurface model for faulting beneath wrinkle ridges has been described as a shallowly rooted fault with a dip angle of 30°, extending to 4.5 km of depth after perhaps propagating upward from one of these stratigraphically weak layers (Schultz, 2000; Watters, 2004).

Lobate scarps are assumed to be underlain by thrust faults that do break the surface, as the boundary between the steep front scarp of the hanging wall and shallow footwall top is typically observed to be sharp and linear (Herrero-Gil et al., 2020; Watters, 1993). Lobate scarps are commonly observed to have high relief, asymmetric topography, and simpler morphologies and planforms than wrinkle ridges (Figures 1c and 1d) (e.g., Mueller & Golombek, 2004). These shortening landforms typically demonstrate a lobe shape as one of its defining characteristics, hence, the name. On Mars, lobate scarps range from tens to over four hundred km in length and have ∼110 to more than 2,000 m of relief (Herrero-Gil et al., 2020; Watters & Robinson, 1999). Although broadly dispersed around the planet, many large lobate scarps are located along the dichotomy boundary and in the highlands of the southern hemisphere, typically observed within thrust belt systems (Klimczak et al., 2018).

Due to their simpler morphology, lobate scarps are often assumed to have simpler structural geometries in the subsurface, usually described as a single anticline overlying a thrust fault. Models of these faults found typical geometries dipping between 20° and 40° (Mueller et al., 2014; Schultz & Watters, 2001). Patterns in fault growth can be informed by the relationship between displacement, calculated as fault (dip) parallel slip, and fault length (Cowie & Scholz, 1992; Schultz et al., 2006), which allows us to conceptualize the fault geometry (e.g., Klimczak et al., 2018). Geometry of the subsurface includes the number and linkage of faults, depth of faulting, and presence of layered rheological barriers that limit downward propagation (Atkins et al., 2022). A common referenced barrier for lobate scarps is the brittle-ductile transition (e.g., Andrews-Hanna, 2020), but some studies show that faults may not extend this depth and imply that lobate scarps may share the listric fault geometries ascribed to wrinkle ridges (Herrero-Gil et al., 2020).

2. Methods

To develop quantitative criteria to categorize shortening landforms on Mars as wrinkle ridges or lobate scarps, we first produced a global dataset of randomly selected landforms to collect information about their surface morphology. We then modeled their subsurface structural geometry to extract subsurface measurements. We combined these parameters to develop a holistic surface-subsurface model and characterized structural geometries and quantities of strain accommodation by each type of landform.

2.1. Selecting Landforms for Analysis

We designed a Geographic Information System (GIS) in ESRI's ArcMap to assist with landform selection and analysis. In our GIS, we utilize the streamed Mars Context Camera (CTX, 5 m/pixel) global mosaic (NASA/JPL/MSSS/The Murray Lab) and overlayed imagery with a semi-transparent, colorized digital elevation model (DEM) from the combined resources of a High-Resolution Stereo Camera (HRSC) and Mars Orbiter Laser Altimeter (MOLA, together 200 m/pixel, Fergason et al., 2018). We then divided the global GIS of Mars into 648 10° longitude by 10° latitude bins.
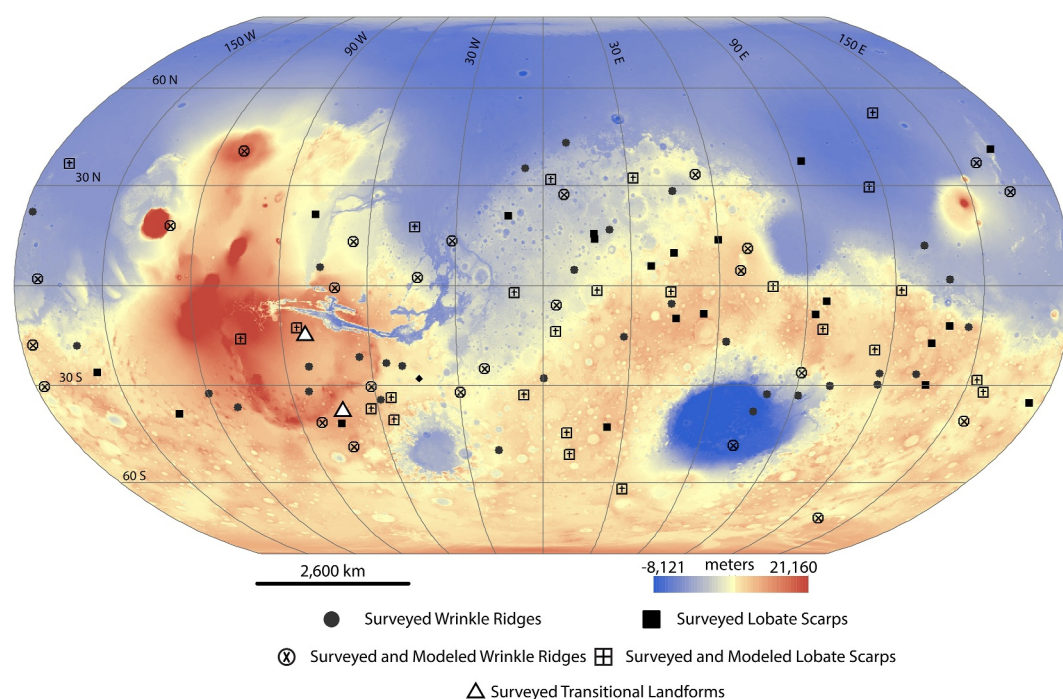
Figure 2. Global distribution of 100 shortening landforms that were surveyed for observational analysis (all symbols). Modeled landforms are distinguished by open symbols. Symbol locations are displayed on the Mars Orbiter Laser Altimeter basemap that is shown in the Robinson projection. Circular symbols depict wrinkle ridges, and square symbols depict lobate scarps. The two white triangles in the Western Hemisphere depict the locations of transitional landforms.

Within each bin, we searched for ∼5 shortening landforms that had sufficient length (>30 km), visually noticeable relief, and image quality such that their surface features could be described in detail. A point was placed along the length of these landforms and saved within a point shapefile to record their locations and assign a feature identification number to each landform. After designating the positions of 998 potential landforms globally, a random number generator was used to select the 100 most representative landforms (one per bin). We specifically selected 100 landforms that would be easily recognized as lobate scarps or wrinkle ridges qualitatively based on descriptions within existing literature (Figure 2). The purpose is to redefine what these landforms could mean and not necessarily to say that they are discrete landform types.

2.2. Surface Morphology Mapping and Measurements

For all selected landforms, a general planform polyline and a detailed set of fault traces were produced during the surface morphology mapping process. The mapping scale was fixed at 1:250,000 and projected to the Mars Sphere (2,000) coordinate system. Shapefiles for planforms (polyline indicating general movement of the fault) and traces were created in the geodatabase. For each landform, more detailed fault trace layers were produced first (black and purple toothed lines, Figure 1). Using the freehand polyline tool, we conducted highly detailed tracing of all the potential fault surface breaks for lobate scarps, which were visually assigned as the sharp topographic transition observed at the base of steep slopes. The inferred blind faults for wrinkle ridges were visually assigned to a less sharp but still observable slope transition adjacent to landform crests. The planform polylines followed the base of the fore-slope or potential surface breaks and were constructed second by using the freehand polyline tool. The goal of creating these features is to capture the overall map pattern of these landforms, whether that be linear to arcuate or straight to sinuous. We aimed to capture average morphological data along the landform length. A script was written to produce a point every 10 km along the length of the mapped faults, approximating where a transect line would need to be drawn. Each transect line was drawn from the beginning of the back limb to the end of the front scarp, making sure to span the total positive relief and thus covering the deformation from the fault(s) in the subsurface. Coordinates and elevation from the transect lines were exported into a spreadsheet for analysis.
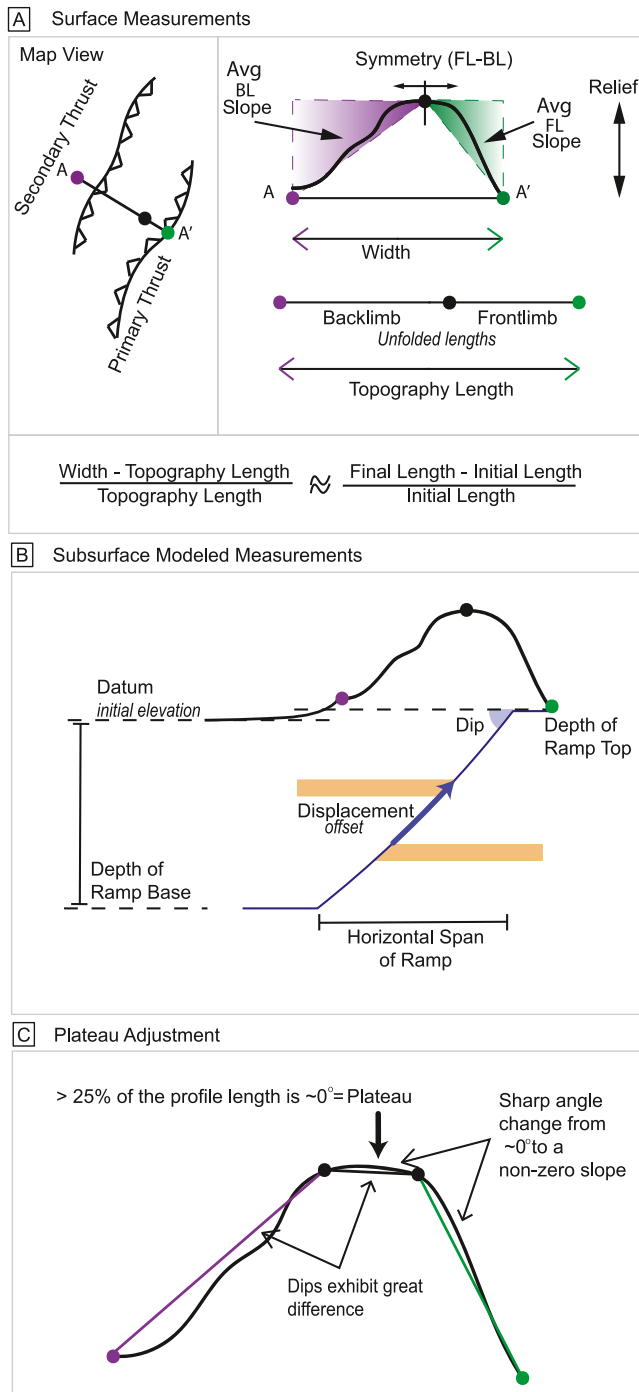
A   Surface Measurements

$$\frac{\text{Width} - \text{Topography Length}}{\text{Topography Length}} \approx \frac{\text{Final Length} - \text{Initial Length}}{\text{Initial Length}}$$

B   Subsurface Modeled Measurements

C   Plateau Adjustment

Figure 3.

We then collected and calculated a suite of surface parameters. Primary measurements included the geographic coordinates of each landform, and map length of the landform from ArcMap. The maximum relief was calculated by subtracting the highest and lowest elevation points along the transect lines (green and black circles, Figure 3a) and reporting the largest value across the transects. The relief-to-length ratio was calculated by dividing the maximum relief by the mapped length. Width was recorded and measured by subtracting the lateral coordinates of end point positions along the profile (purple and green circles, Figure 3a). Maximum width along each landform was recorded. As symmetry is often cited as a component of shortening landform qualitative definitions, we calculated the slope of the forelimb (green shaded angle) and back limb (purple shaded angle) and considered the ratio of the two values to be a representation of symmetry, where the nearer the ratio to one, the more symmetrical the landform. Average values of each parameter were recorded for each landform. The forelimb length was the length of the limb in the front of the structure; the back limb length was taken from the limb on the back of the structure. Total profile length was the sum of both limbs, and strain was calculated by quantifying the ratio between the total topography length (i.e., initial length) and width (i.e., final length). We also included a column of what landform classification we determined each to be based on existing literature: wrinkle ridge or lobate scarp.

Sixty-three profiles out of the hundreds drawn showed wide plateaus at peak elevations. These plateaus were removed from calculations of back limb and front limb slope but included for calculations of width and total topographic length. If landforms included plateaus, starting and ending points for the plateau (black circles, Figure 3c) were used instead of a single peak point for slope and limb length calculations.

A Discriminate Function Analysis (Discriminant Function Analysis (DFA), detailed methodology discussed in Section 2.4) was carried out to statistically determine a model to define morphological differences between the observed lobate scarps and wrinkle ridges. Results of DFA include probabilities of the landforms studied being correctly grouped into their assigned classes. Landforms with the highest probabilities are exemplars of their group ("poster children" for lobate scarps and wrinkle ridges). We used 25 wrinkle ridges and 25 lobate scarps with the highest probabilities of being correctly classified in our analysis of subsurface geometry. This way, the most representative subsurface geometries for each category could be captured.

2.3. Subsurface Structure Estimations

We modeled the subsurface structural architecture of 50 landforms (open symbols in Figure 2) using the MOVE Structural Geology Modeling Software

Figure 3. Conceptual diagram of the measurements performed. (a) A transect drawn perpendicularly across a wrinkle ridge. Purple and green circles indicate locations where deformation was no longer observed in the topography at the base of the back and front limbs, respectively. The black circle is the point with the highest elevation in the profile. Symmetry, back limb and front limb slope, relief, width, back limb and front limb length, and undeformed topographic length are also represented. Our calculation for longitudinal, not total, strain is also provided. (b) Values collected when modeling the subsurface showing the elevation datum, depth to the top of the fault ramp, dip, displacement, depth to the base of the fault ramp, and structural width. (c) Plateaus (flat region between black circles) were removed from slope calculations when >25% of the profile length had a slope near zero.
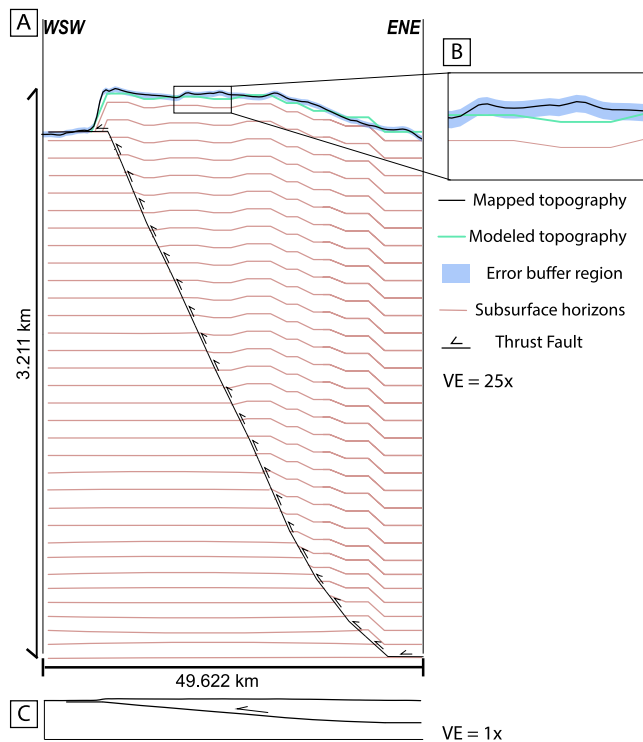
Figure 4. A 2D transect of a landform modeled in MOVE (a). The Mars Orbiter Laser Altimeter topographic profile (black) is shown with the forward modeled topography (teal line), with the buffer zone that defines a successful model surrounding both (blue region). Deeper stratigraphic horizons are shown in pink, and the thrust fault is indicated by black lines with arrows. The vertical exaggeration is 25x for both the topographic profile and the subsurface structure. In order to show the modeled and actual topography within the buffer zone in detail, a close-up image is provided (b), and to assist in visualizing the scale of the fault and landform, both are also shown with 1x vertical exaggeration (c).

provided by Petroleum Experts. MOVE allows for 2D and 3D modeling of fault surfaces in geologically and geographically realistic contexts. Forward modeling modules within the package allow users to define movement along these surfaces to derive properties such as surface elevation changes, multi-dimensional strain, and folding geometries above the upper ramp edge. For accommodating shortening strains, MOVE permits modelers to specify the folding mechanism with which materials deform during slip such as fault-bend folding and fault-propagation folding. Fault-bend folding was applied in our study. Although this software was originally intended to analyze terrestrial data, data from Mars, Mercury, and other planets can be imported by changing the projection of the software visualization window (e.g., Crane, 2020) so that planetary datasets imported into MOVE are scaled and displayed with their correct frames of reference.

We extracted imagery and DEMs to the extent of each landform. Data were projected in ArcMap using stereographic projections centered on each landform with a Mars 2,000 spherical reference frame, and then MOLA DEM and CTX images surrounding the entirety of the landform were exported. These files were saved as geotiffs, and then imported into MOVE. The imagery was draped over topography, and the 3D surfaces perpendicular to the landform trend were vertically sliced using the "Create Section" tool. This tool allows a user to specify the depth, elevation above the surface, and orientation of a cross section, which when created, will only contain the topographic profile of the transected DEM. The transect was preferentially drawn across the region of the shortening landform with the highest quality imagery and most characteristic topography based on previous literature descriptions of each type of landform and morphology (e.g., Andrews-Hanna, 2020; Banks et al., 2012; Mueller & Golombek, 2004; Watters et al., 1988). Transects were long enough to encompass the entire back slope and front slope so that any positive relief associated with deformation would be represented along the topographic profile (black line, Figure 4), but we acknowledge that this approach does not account for possible negative relief that could be associated with deformation such as trailing or leading synclines. None of such features were noted in this study. Subsequently, each section was opened in a unique 2D modeling visualization window.

We then forward modeled the topographic and structural development of the landform in 2D along the created transect. The "Construct Horizons" tool was used to create reference horizons with horizon tops every 20 m (pink lines, Figure 4). The uppermost horizon was level with the base of the foot wall (i.e., the level surface foreland of the steep front slope). The elevation of this surface was recorded. Reference horizons are not assumed to have laterally or vertically varying mechanical properties, but instead are helpful because they allow for displacement to be visualized and measured along the fault surface. Each horizon line is composed of equally spaced vertices (250 m apart). Deformation (faulting and folding) of the uppermost horizon results in elevated topography, which can be compared with the observed landform topography assuming negligible erosion.

MOVE does not have an automated iterative mechanism for testing different fault geometries, so the user must manually edit the fault geometry between each model run. We reflected on predicted geometries for the surface folding expression above thrusts to aid in the ways we edited the fault (Chester et al., 1991; Medwedeff & Suppe, 1997; Mitra, 2002; Suppe, 1983). The algorithm assumes that the horizons in the hanging wall block are displaced during fault-bend folding and does not deform the footwall rocks. Using the fault-bend folding algorithm, we developed topography above a thrust, manually iteratively changing the position of the upper and lower ramp transitions, fault dip, displacement (increased in 100 m increments), and presence or absence of a transition to a horizontal fault at depth. Faults were initially drawn in the subsurface with 30° dip, as this fault dip is associated with previous modeling efforts (i.e., Schultz & Watters, 2001; Okubo & Schultz, 2004; Egea-Gonzalez et al., 2017) and is predicted from Andersonian Mechanics (Anderson, 1951; Jaeger et al., 2009). MOVE applies slip along these dipping faults to predict the resulting topography following Suppe (1983) and Mitra (1990), as

discussed in Brandes and Tanner (2014). Unlike Coulomb Modeling (Lin & Stein, 2004; Toda et al., 2019), MOVE explicitly includes deformation from plastic folding and therefore allows the user to decompose horizontal and vertical components of shortening associated with faulting and folding. Fault dips were adjusted iteratively between model runs to improve agreements between the observed and forward modeled topography, starting at 30° and reducing by 2° per run. The upper ramp edge was initially aligned with the base of the front slope (thick black line with arrows, Figure 4), a simple geometry implied by thrust faults of Earth (Laubscher, 1985; Robinson et al., 2006), the observations of thrust fault surface breaks on other planetary bodies (Klimczak et al., 2018; Schultz et al., 2010), and previous modeling efforts on Mars and Mercury (Crane & Klimczak, 2019b; Crane, 2020; Rich, 2023). The upper ramp edge was lowered by 1 km per run as necessary. The lower ramp edge was initially aligned horizontally with the backlimb topographic transition to the profile datum (with depth determined by the initial 30° dip. This transition point was also adjusted up or down by 1 km per run as necessary. Kinks in the fault ramp, which gave the fault a more listric or concave geometry, were added when needed to reproduce topographic signatures. They were preferentially located below dramatic changes in topography and smoothed as necessary to bring the modeled topographic profile into agreement with the observed profile. After each adjustment, the Preview function was used to assess the model geometry.

While MOVE is capable of forward modeling shortening from fault-propagation folding, fault parallel flow, simple shear, and trishear folding, we selected fault-bend folding because this algorithm accounted for folding (unlike simple shear and fault parallel flow), while limiting complications due to specialized limb angle and hinge ratios (unlike trishear and fault-propagation folding). It made no assumptions about the rate of fault growth with fold development (unlike fault-propagation folding; Mitra, 1990) or about the ability for deformation to be translated into the foreland (Chester et al., 1991). Furthermore, fault-bend folding has been previously identified as an appropriate kinematic model for upper crustal structures in fieldwork and seismic observations on Earth (i.e., Brandes & Tanner, 2014; Hughes et al., 2014). The fault-bend folding algorithm assumes that folding is parallel to faulting with anticlinal folds developing over kinks in the fault plane, and that unit thickness, line length, and unit area are preserved (e.g., Suppe, 1983). This quality implies that direct geometrical implications for the fault plane can be deduced from the surface topography of the overlying landform (Connors et al., 2021; Suppe, 1983). Fault-bend folding is more appropriate for symmetrical landforms (Hughes et al., 2014), whereas fault-propagation folding is a more appropriate model when there are greater differences between front and backlimb slope or when the front limb is overturned (Shaw et al., 2005). Also, both types of models can account for folding above blind faults, while fault-bend folding can also account for surface-breaking faults as the upper ramp flat may propagate toward the foreland and break the surface (Hughes & Shaw, 2014; Suppe, 1983; Suppe & Medwedeff, 1990). Due to its simplicity and the connections between surface topography and fault plane geometries, the fault-bend folding algorithm is most appropriate for low angle faults, and our study therefore estimates lower bounds on fault dips. Lower fault dips will require more displacement in order to achieve the elevated topography associated with shortening landforms, and therefore, the displacement associated with this study can be considered a maximum. Together, low dips and high magnitude displacements can help us identify a thin-skinned end member model for landform structural geometry and determine if there are quantifiable structural differences in wrinkle ridges and lobate scarps.

Successful models were defined by reproducing >50% of the surface topography within nearly 20 m of vertical precision along the entire landform topography including the full backlimb, max relief, and front scarp. In previous modeling efforts (e.g., Watters, 2004), replication of topography has been used as a criterion for model success, and so we use that in this work as well. We used the "Construct Horizons" tool to draw a 20 m buffer zone around the observed topographic profile (blue region, Figure 4). After each model was produced, we visually assessed if >50% of the modeled topography was within this buffer zone and confirmed that no large topographic artifacts were produced in the model. This same method was applied in Crane (2020) for modeling shortening landforms on Mercury. Once the modeled topography sufficiently matched the observed topography, we deemed the model successful and recorded the parameters associated with the fault geometry and structural history. The model parameters were used in a statistical analysis to determine differences between lobate scarps and wrinkle ridges.

2.4. Statistical Method

To statistically differentiate between wrinkle ridges and lobate scarps, we performed three Discriminant Function Analyses (DFAs) using R (Crawley, 2015). A DFA is a multivariate technique that creates a linear function to

distinguish samples between predefined groups along multiple dimensions. A linear function is constructed from the observed variance of measurements across a set of input samples. The DFA is then used as a way to predictively categorize previously unsorted samples (e.g., Kovarovic et al., 2011). The first DFA was constructed from only morphological properties observable in surface data, the second DFA was constructed from measurements obtained from modeled fault geometries, and the third DFA incorporated both sets of observational and modeled parameters to create a holistic assessment of landforms based on both surface and subsurface properties. A DFA is a parametric statistical analysis and therefore requires normality across all of the input data. Some measurements (those indicated with an asterisk in Table 1) were natural logarithmically transformed before the DFAs were completed. Other assumptions of a DFA include that landforms can only belong to one group, and that each landform is structurally independent of other landforms. To confirm these assumptions, we selected landforms for study that could be confidently qualitatively categorized as wrinkle ridges and lobate scarps, and that were distributed around the globe (see Section 2.1).

In a DFA, loadings are attributed to each measurement type (bold, Table 1). The larger the absolute value of each loading, the more influence that measurement has on the DFA, as these loadings are used in the linear functions as coefficients on each of the input sample's measurements. This allows us to assess which measurements are most influential in dictating what category a shortening landform belongs to.

The resulting value that is used to distinguish one group from another in a DFA is a linear discriminate (LD). When assessing two groups with a DFA, larger positive LD values would correspond to samples being more confidently assigned to one group, while more negative values would correspond to samples being more confidently assigned to the other group. Samples that produce LD values in an intermediate range may exhibit qualities of both groups such that it is difficult to confidently determine in what group that sample resides in.

Shortening landforms that produced the highest and lowest LD values were most likely to be classified as one landform type or the other, permitting us to distinguish the individual landforms which best exemplified the characteristics of their group. After running the DFA for the surface morphological distinctions, these predictive statistics were used to select the 25 wrinkle ridges and 25 lobate scarps that most clearly represented these classifications. These 50 landforms were then used to model subsurface characteristics for the groups.

3. Results

3.1. Surface Morphology

The DFA performed on surface morphology variables alone showed that the three most important parameters for classifying shortening structures are maximum width (coefficient of 1.43), forelimb slope (coefficient of −1.06), and back limb length (coefficient of −1.25). Because these coefficients are derived from logarithmically transformed datasets, it is more physically meaningful to report and discuss untransformed means and standard deviations for these variables for our sampled landforms (Table 1). Note that some standard deviations are large, which is due to our selection of a wide range of landform sizes and morphologies and because size distributions (such as length and width) tend to have long right tails. In skewed distributions, a standard deviation less than the mean can sometimes result in a negative value. Obviously, these negative lengths, widths, and other parameters are not realistic and the minimum value encompassing a standard deviation should be taken to be zero in these cases. To assist in visualizing the spread of important variables, we include multiple box and whisker plots in Figure 5 (discussed below).

Our sampled lobate scarps tend to have a greater width, averaging 34 ± 38 km, while wrinkle ridges tend to be narrower landforms, averaging a width of 29 ± 27 km. Lobate scarps have steeper forelimb slopes compared with wrinkle ridges. For our sample, these slopes average $4.3° \pm 3°$, whereas the front limbs of wrinkle ridges tend to slope $2.8° \pm 2.3°$. Lobate scarps have a longer back limb, averaging 13.1 $\pm$ 13.9 km. Wrinkle ridge back limbs average 9.3 ± 11.4 km in length. The longer lengths and larger widths associated with lobate scarps indicate that these landforms might accommodate more strain. While the linear coefficient of the model produced by the DFA also implies that lobate scarps accommodate more strain (−0.102), this coefficient was not statistically significant. The average absolute longitudinal, not total, shortening strain for wrinkle ridges was $0.16\% \pm 0.32\%$ and $1.4\% \pm 6.5\%$ for lobate scarps. Other variables, such as length and relief-to-length ratio, did not differ significantly across surface measurements.

Table 1
Surface Parameter Averages for the 100 Sampled Landforms

	[a]*Length of Landform* (km)	[a]*Maximum Relief: Length* (unitless)	[a]*Maximum Relief* (m)	[a]*Maximum Width* (km)	[a]*Forelimb Slope* (degrees)
Wrinkle Ridge AVG	120 ± 80	0.003 ± 0.002	250 ± 160	29 ± 27	2.8 ± 2.3
Lobate Scarp AVG	106 ± 108	0.005 ± 0.003	480 ± 620	34 ± 38	4.3 ± 3.0
LD1 Coefficients	0.409	−0.634	−0.076	**1.56**	**−1.03**
	[a]**Back limb Slope** (degrees)	[a]**Symmetry** (unitless)	[a]**Forelimb Length** (km)	[a]**Back limb Length** (km)	[a]**Total Profile Length** (km)
Wrinkle Ridge AVG	1.7 ± 1.7	0.07 ± 0.22	6.2 ± 2.9	9.3 ± 11.4	17.1 ± 14.7
Lobate Scarp AVG	1.9 ± 1.6	0.07 ± 0.10	9.3 ± 15.2	13.1 ± 13.9	22.7 ± 24.2
LD1 Coefficients	0.318	0.069	−0.402	**−1.34**	−0.195
	[a]**Average Strain** (%)	[a]**Average Front limb/Back limb** (unitless)			
Wrinkle Ridge AVG	−0.16 ± 0.32	2 ± 1			
Lobate Scarp AVG	−1.4 ± 6.5	1 ± 0.7			
LD1 Coefficients	−0.094	−0.315			

[a]Natural logarithmically transformed.

Based solely on surface morphometrics, shortening landforms can be classified correctly 79% of the time. The average value for the linear discriminant for wrinkle ridges was 0.84 ± 0.80 and for lobate scarps was −1 ± 0.6, implying that these distributions are not expected to overlap within one standard deviation of each other (histogram A, Figure 6). Some landforms have linear discriminants within the alternate classification range, demonstrating the spectrum of values possible for landform characteristics, which could be a useful classification system for differentiating more endmember styles of landforms. However, defining features makes accurate classification possible most of the time for our sampled landforms. Surface parameter averages are provided in Table 1. To visualize the ranges for these parameters, box and whisker plots for the variables found to be most important for distinguishing landforms at the surface are shown in Figure 5a.

3.2. Subsurface Structure

The DFA for subsurface structural geometry emphasized the importance of dip and depth of faulting in differentiating the landforms (box and whisker plots, Figure 5b). The linear coefficient for dip was −0.824, indicating that lobate scarps are characterized by more steeply dipping faults than wrinkle ridges. Faults underlying lobate scarp dip an average of 5.3° ± 2.2°. Wrinkle ridges are underlain by shallower faults, dipping 3.7° ± 1.6°. The linear coefficient associated with the depth of faulting was −0.861, indicating that lobate scarps extend deeper into the subsurface, with an average depth of 1,810 ± 2,610 m. Wrinkle ridge faults are typically observed to extend to depths of 790 ± 810 m. Based on all measured subsurface parameters, landforms were classified correctly 70% of the time (histogram B, Figure 6).

Displacement was not an important variable differentiating the two types of landforms (coefficient of −0.00205). The horizontal component of displacement, called heave, was calculated for each fault. By comparing throw, the distance the lithosphere shortened at the surface, with initial undeformed topographic length collected from the surface model, we calculated strain percentages from modeling. The average absolute longitudinal shortening strain from modeling for wrinkle ridges was 15% ± 9%, and for lobate scarps, these values were 17% ± 10%. Both types of landforms represent similar shortening strain percentages. These values and the parameter averages for subsurface characterization are reported in Table 2.
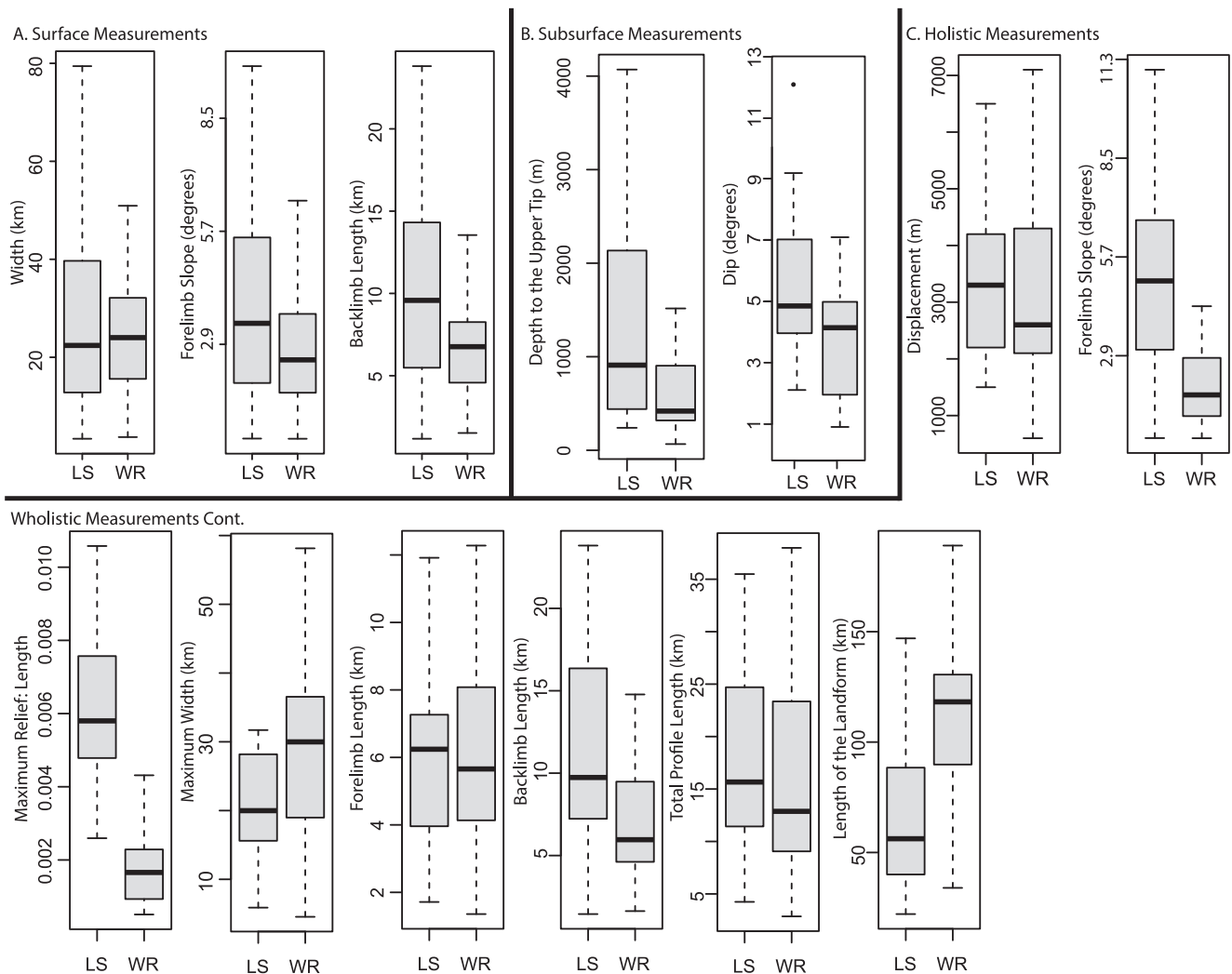
Figure 5. Box and whisker plots show the distribution of non-transformed surface and subsurface measurements that help distinguish wrinkle ridges and lobate scarps for the (a) mapped 100 landforms used in the first Discriminant Function Analysis (DFA) and modeled 50 landforms used in the subsurface (b) and holistic DFA models (c).

3.3. Holistic Model

We unified our surface and subsurface metrics in order to conduct a DFA that would produce a holistic, linear model to differentiate landforms in their entirety. We found that maximum width, forelimb length, back limb length, and total profile length were all driving differences between the landform types (Table 3 and summarized in plots in Figure 5c). We also found that the distributions of LD values for each DFA differ greatly from one another (Figure 6). All of the most influential parameters to distinguish shortening landforms into landform types relate generally to the expanse of the landforms perpendicular to the direction of faulting and indicate that lobate scarps are overall wider landforms than wrinkle ridges (Figure 5).

Length, relief-to-length ratios, and depth of faulting are also different between wrinkle ridges and lobate scarps in a holistic model (Figure 5c). Wrinkle ridges have lower relief-to-length ratios and values indicate that surface expressions are more subtle than for lobate scarps. Wrinkle ridges and lobate scarps that have similar relief are different in that wrinkle ridges are typically longer landforms than lobate scarps but lobate scarp faults extend to deeper depths based on our models. Using surface morphology and modeled subsurface geometry, landforms could be classified correctly 96% of the time (Figure 6c).
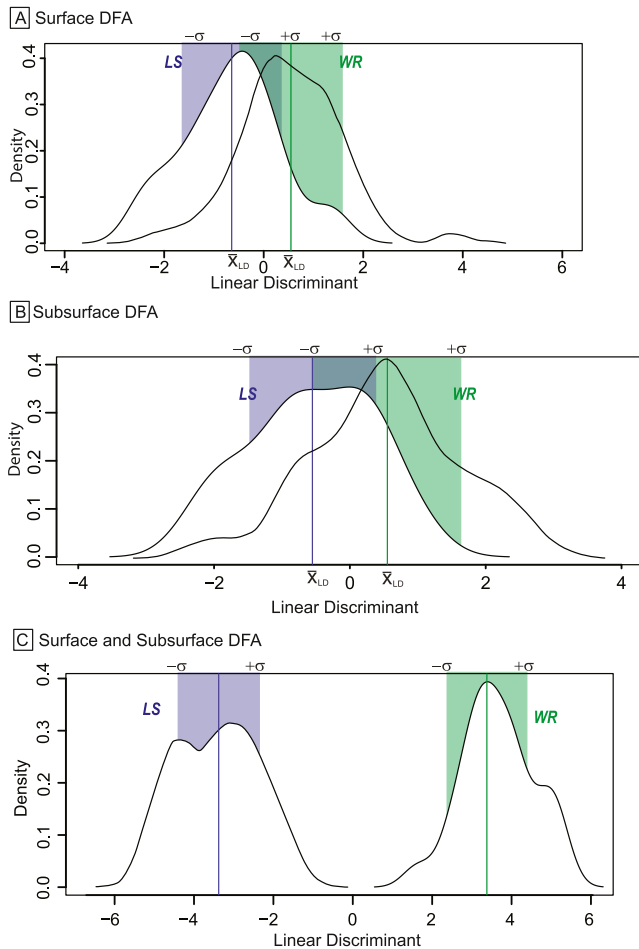
Figure 6. (a) Surface morphology, (b) subsurface geometry, and (c) holistic model analyses derived from discriminant function analysis. Linear discriminants (the model value for each landform) are plotted for lobate scarps (blue) and wrinkle ridges (green). Dark blue and green lines represent average linear discriminants for each landform type, and standard deviations of these values are bounded by blue and green boxes. The wide gap between the color regions in panel (c) demonstrates the success of analyzing landforms at the surface and in the modeled subsurface when aiming to classify the landform types.

4. Discussion

Our results confirm that there are quantifiable differences between wrinkle ridges and lobate scarps on Mars, but more importantly, these measures serve to influence our estimates of shortening, interpretation of how these landforms accommodate shortening, and when combined with lithological or timing context—how those mechanisms change across space and time. We recognize that by defining the end members for each landform population, our results reflect the quantitative classification of ideal shortening landforms. Many shortening landforms can fall on a spectrum between lobate scarp and wrinkle ridge endmembers (e.g., Figure 6a), but we suggest that they can still be classified using the model presented here.

Modeled faults underlying wrinkle ridges tend to dip less steeply, albeit only by a few degrees, which means that as they accumulate displacement, much of this is translated horizontally, and topographic development is more subtle. This leads to underestimating shortening when inferring strain from vertical relief measurements and fault lengths alone; however, the widths of the landforms imply that the subsurface faults are extensive (wide, long, and branching) even if they are not deep. As strain accumulates, it is largely accommodated through folding and horizontal motion along shallow faults. The shallowly sloping limbs of the landforms imply that deformation that leads to building the topography of wrinkle ridges is best described by fault-bend folding, where fold geometry mimics fault geometry at depth (as expected by Suppe (1983)). We note that this method provides lower bound estimates of fault dip and upper bound estimates of displacement. While the structural models therefore represent limits of reasonable fault geometries, they accomplish a major goal-demonstrating that structural architectures of and the shortening accommodated by these landforms likely differ.

Wrinkle ridge faults grow from a narrow range of shallow depths and continue to propagate lengthwise without gaining significant relief, resulting in modest relief-to-length ratios. This implies that there may be significant lithological barriers at depth that prompt the formation of wrinkle ridges over lobate scarps. An alternative explanation is that the sources of stress associated with wrinkle ridge formation primarily affect the uppermost portion of the lithosphere.

Lobate scarps are characterized by slightly steeper thrusts that propagate deeper into the lithosphere. Due to marginally steeper fault dips, displacement accumulates vertically to a greater extent than expected for wrinkle ridges. This added vertical displacement results in more dramatic topographic pro-

Table 2
Modeled Subsurface Parameter Averages for the 50 Sampled Landforms

	[a]*Displacement* (m)	*Initial elevation* (m)	*Depth to ramp top* (m)	*Dip* (degrees)	*Horizontal span of ramp* (km)
Wrinkle Ridge AVG	3,290 ± 2,560	380 ± 4,000	380 ± 3,870	3.7 ± 1.6	22 ± 21
Lobate Scarp AVG	4,480 ± 4,160	530 ± 3,190	320 ± 3,190	5.3 ± 2.2	39 ± 69
LD1 Coefficients	−0.307	0.0000173	**−1.17**	**−0.861**	0.828
	[a]*Depth to Ramp Base* (m)	*Shortening Strain* (%)	*Strain Shortening* (m)		
Wrinkle Ridge AVG	790 ± 810	15 ± 9	3,400		
Lobate Scarp AVG	1,810 ± 2,610	17 ± 10	4,900		
LD1 Coefficients	−0.204	Not included in the DFA directly	Not included in the DFA directly		

[a]Natural logarithmically transformed.

Table 3
Holistic Parameters for the 50 Modeled Landforms

	[a]*Displacement* (m)	*Initial elevation* (m)	*Depth to ramp top* (m)	*Dip* (degrees)	*Horizontal span of ramp* (km)
Wrinkle Ridge AVG	3,290 ± 2,560	380 ± 4,000	380 ± 3,870	3.7 ± 1.6	22 ± 21
Lobate Scarp AVG	4,480 ± 4,160	530 ± 3,190	320 ± 3,190	5.3 ± 2.2	39 ± 69
LD1 Coefficients	**0.550**	−0.000153	**−0.643**	0.395	0.242
	[a]*Depth to Ramp Base* (m)	[a]*Length of Landform* (km)	[a]*Maximum Relief* (m)	[a]*Maximum Relief: Length* (unitless)	[a]*Maximum Width* (km)
Wrinkle Ridge AVG	790 ± 810	128 ± 7,245	197 ± 116	0.0017 ± 0.001	31 ± 23
Lobate Scarp AVG	1,810 ± 2,610	76 ± 53	553 ± 636	0.007 ± 0.003	32 ± 36
LD1 Coefficients	*0.557*	*0.974*	−0.147	*−1.726*	*2.532*
	[a]*Forelimb Slope* (degrees)	[a]*Back limb Slope* (degrees)	[a]*Symmetry* (unitless)	[a]*Forelimb Length* (km)	[a]*Back limb Length* (km)
Wrinkle Ridge AVG	2.1 ± 1.3	1.4 ± 1.0	0.093 ± 0.327	6 ± 3	8 ± 6
Lobate Scarp AVG	5.0 ± 2.7	1.8 ± 1.2	0.07 ± 0.05	10 ± 19	14 ± 14
LD1 Coefficients	*−2.214*	*0.607*	0.412	−0.434	*−3.733*
	[a]*Total Profile Length* (km)	[a]*Average Strain* (%)	[a]*Average Front limb/Back limb* (unitless)		
Wrinkle Ridge AVG	16 ± 9	−0.1 ± 0. 3	1.33 ± 0.782		
Lobate Scarp AVG	25 ± 29	−2.5 ± 8.8	0.837 ± 0.495		
LD1 Coefficients	0.487	−0.247	*−1.690*		

[a]Natural logarithmically transformed.

files, contributing to higher (but still incomplete) strain estimates from topography alone. Lobate scarps represent on average, the same strain percentages as wrinkle ridges when calculated from modeled heave estimates, and this difference implies that faulting plays a more important role in lobate scarp deformation than it does for wrinkle ridge development. Because lobate scarps are overall larger landforms, these equivalent strain percentages translate into greater amounts of shortening, around 1.5 additional km on average for our lobate scarps (Table 2).

Dip and depth generally relate to landform and fault growth mechanisms, and overall, our results may indicate that the faults underlying lobate scarps grow uninhibited while the faults below wrinkle ridges may be interrupted by vertical rheological layering and mechanical boundaries at depth, which have been shown to affect fault displacement and length relationships (e.g., Cowie & Scholz, 1992). Thus, wrinkle ridges accumulate length without gaining considerable amounts of relief that arises from bringing rock materials up along fault ramps from depth. For these landforms, shortening strain is accommodated by building some relief but is compensated with greater growth along the ramp edges.

The large variations in displacement, depth, and strain from modeling associated with lobate scarps implies that these features are observed at multiple stages of maturity, an inference that allows us to make interpretations of fault propagation characteristics. Unlike wrinkle ridges, lobate scarps have a broad range of depths to their lower ramp transitions, which may imply that they can propagate from a wide variety of depths and unit types. Therefore, their relief and length are restricted by strain rates and the longevity of the stresses that prompt their growth—not their physical or lithological setting. Faults are known to grow by the linkage of cracks into larger slip surfaces (Cowie & Scholz, 1992), which results in fault populations with large numbers of small faults and

exponentially smaller quantities of large faults. Over time, the fault population evolves, and linkage may continue, increasing the number of longer (i.e., mature) faults. This is what we may have observed with the wrinkle ridge length distribution-that wrinkle ridges represent a population of faults that reached maturity and evolved coevally. Co-evolution and propagation from a decollement or weak layer may explain why wrinkle ridges are often arranged with periodic spacing (e.g., Watters, 1988). These structures have simply reached maturity as a population. Lobate scarps, however, represent a range of maturity. Therefore, we hypothesize that lobate scarps and wrinkle ridges accommodate different magnitudes of strain on different timescales. This hypothesis could be tested with statistical tests capable of incorporating ordinal and nominal variables such as lithology, estimated lithospheric strength, and age, such as a Spearman's Rank test (Gauthier, 2001).

4.1. Fault Dips and Depths: Modeling, Previous Studies, and Earth Analogs

Our results also call into question fault dip and depth estimates from previous works. Past modeling efforts have found fault dips that predominantly range from 25° to 40° (e.g., Ruj et al., 2018; Schultz & Watters, 2001; Williams et al., 2013), with the exception of two studies by Herrero-Gil et al. (2019, 2020) who found that the fault underlying Bosporos Rupes dips ~23° and some backthrusts associated with the Ogygis Rupes system to dip ~22–23°. Those authors considered folding during deformation by applying a trishear model for fault and fold development. Their derived dip is shallower than previous modeling efforts, but is still steeper than those presented in our study. This discrepancy may be explained by the very large scale of the lobate scarps that they modeled and that the trishear algorithm allows for folding over steeper faults to produce gentle limb slopes. Works that applied Coulomb modeling (Toda et al., 2019) to derive dip and depth do not explicitly consider plastic folding, which may account for over-steepened fault dips. In either case, we advocate for future works to contribute to our community's construction of accurate mental models of faulting by presenting surface topography and faults with equal vertical exaggeration (Figure 4c). Although other studies may have applied equal exaggeration to topography and fault dips during modeling, displaying exaggerated topographic profiles of the landform surface with unexaggerated fault dips may contribute to community misunderstandings about the connections between surface and subsurface geometries.

On Earth, faults associated with major orogenic systems are observed to dip shallowly, especially with depth. We therefore believe it is important to reflect on field experience and observations of thrust systems accommodating folding in order to evaluate the accuracy and realism of models for other planetary structures. For example, the intraplate frontal thrusts associated with the Ouachita Mountains of Arkansas and Oklahoma (i.e., the Y-City, Ross Creek, and Ti Valley thrusts) have dips which have been observed to be 10°–50° at the surface and transition into very shallow dips at depth (Kaspar Arbenz, 2008). Intraplate earthquakes in other systems indicate dips between 20° and 50° (North America broadly, depths <29 km; Zoback, 1992), and ~25°–30° in the Yakima Fold Belt analogue region (Crane & Klimczak, 2019a; Kelsey et al., 2017).

Even shallower thrusts are observed at plate and paleoplate boundaries. Appalachian thrusts are characterized by accompanying folding, especially in the Valley and Ridge Provinces. Thrusts such as the Great Smokey Mountain Thrust have been observed to dip 10°–40° while frontal thrusts include: the Appalachian Frontal Thrust (3°, Sak et al., 2012), the Taconic Frontal Thrust (7°, Bosworth et al., 1988), the Brevard Fault Zone (15°–20°, Hawman et al., 2000), and the Blue Ridge Fault (10°–20°, Bailey et al., 2002). In the Himalayan Range, similar shallow dips on frontal thrusts associated with folding are observed at the surface and in seismic profiles (e.g., 10° on the Main Himalayan Thrust, Searle et al., 2006). These shallow dips observed in thrust systems on Earth are substantially less than the 30° dip predicted by the Coulomb Failure Criterion; however, they reflect the realities of deformation in rock mass-that when a rock is critically fractured (as is the entire crust of Earth; Zoback, 2007), that rock will fail at a shallower angle than expected for intact rock. Although plate boundaries are not observed on Mars, it is possible that the rock mass qualities of reused and reactivated fractured orogenic boundaries on Earth are similar in strength to the extensively fractured bedrock in a heavily impacted lithosphere, if in no other way that both are weakened repeatedly over time. Another important feature of these shallow thrusts is the overall shallow forelimb slope observed and predicted (by Suppe (1983) and other models) to be associated with the thrusts. Steeper faults are predicted to result in steeper front slopes. In contrast, the selected landforms for this study had very shallow forelimb slopes (~5°), which contributed to a model fit of shallow dip.

We also note that previous modeling studies assume that the depth of faulting indicates the depth to the Brittle-Ductile Transition (e.g., Egea-González et al., 2017; Grott et al., 2007; Herrero-Gil et al., 2019). Although we

agree that this does in fact indicate a maximum depth of faulting (as this is the deepest that brittle deformation can occur), these depths (>20–30 km in most cases) may be overestimated. As previously modeled faults are larger than those included in this study, they are expected to extend to deeper depths than the thrusts we model. On Earth, faults in major orogenic systems such as the Appalachians and Himalayas are observed in seismic data to extend to 2–10 km depth (Hawman et al., 2000; Searle et al., 2006). In fact, the only thrust faults that extend all the way to the Brittle Ductile Transition on Earth are root faults and sutures facilitating plate collision. In examining the dips of these sutures, we can again reflect on the potential dips of large thrust systems. In the Ouachitas, the mantle suture that allowed for the collision of the Sabine block with Laurentia has been inferred in seismic data to dip 15° (Heron et al., 2019). The suture zone utilized by Gondwana along the southeastern margin of Laurentia is preserved in the southeastern US and is also observed to dip shallowly (3–15°; Hooper et al., 2016), and seismically active lengths of subduction zones, another form of plate suture, are also observed in seismic data to dip shallowly (2–7.5°, Hayes et al., 2012; Lay et al., 2018). We believe that reflecting on available observations from Earth can only improve our understanding of the tectonics of other planets and help constrain future modeling efforts.

5. Conclusions

This work addresses the longstanding question of whether shortening landforms on Mars can be quantitatively differentiated as lobate scarps or wrinkle ridges, and if so, can we determine what drives these differences? We produced a geodatabase of shortening landforms by globally mapping 100 faults and 2D modeling a subset of 50 exemplar fault systems. A DFA provides a model that can rigorously sort these shortening landforms based on their surface morphology and subsurface geometry. Through conducting this study, we have uncovered that morphological differences in lobate scarps may relate to their broader range of fault-evolutionary stages and considered the effects of vertically exaggerated data and Earth analogue information on interpretations in general. This research can facilitate community investigations of the more specific roles that strain, timing, stress sources, and lithology can play in how these shortening landforms record the overall geological history of Mars.

Data Availability Statement

Data produced by this study include: a geodatabase of landforms, spreadsheets of surface morphology measurements for each landform, model workbooks for MOVE structural geology modeling software for each landform, a spreadsheet of surface and subsurface parameters for every landform, and R code for running DFAs that accepts the spreadsheets as inputs. This data is available in the Zenodo Repository (McCullough et al., 2023). MOVE structural modeling software was used under a 2022 free academic license.

References

Anderson, E. M. (1951). The dynamics of faulting and dyke formation with applications to Britain. https://doi.org/10.1017/S0016756800065493

Andrews-Hanna, J. C. (2009). A mega-landslide on Mars. *Nature Geoscience*, *2*(4), 248–249. https://doi.org/10.1038/ngeo483

Andrews-Hanna, J. C. (2020). The tectonic architecture of wrinkle ridges on Mars. *Icarus*, *351*, 113937. https://doi.org/10.1016/j.icarus.2020.113937

Atkins, R. M., Byrne, P. K., Bohnenstiehl, D. R., & Wegmann, K. W. (2022). A morphometric investigation of large-scale crustal shortening on Mars. *Journal of Geophysical Research: Planets*, *127*(5), e2021JE007110. https://doi.org/10.1029/2021JE007110

Bailey, C. M., Giorgis, S., & Coiner, L. (2002). Tectonic inversion and basement buttressing: An example from the central Appalachian blue ridge province. *Journal of Structural Geology*, *24*(5), 925–936. https://doi.org/10.1016/S0191-8141(01)00102-X

Banks, M. E., Watters, T. R., Robinson, M. S., Tornabene, L. L., Tran, T., Ojha, L., & Williams, N. R. (2012). Morphometric analysis of small-scale lobate scarps on the Moon using data from the Lunar Reconnaissance Orbiter. *Journal of Geophysical Research: Planets*, *117*(E12). https://doi.org/10.1029/2011JE003907

BellIII, J. F., Malin, M. C., Caplinger, M. A., Fahle, J., Wolff, M. J., Cantor, B. A., et al. (2013). Calibration and performance of the Mars reconnaissance orbiter context camera (CTX). *International Journal of Mars Science and Exploration*, *8*, 1–14. https://doi.org/10.1555/mars.2013.0001

Bosworth, W., Rowley, D. B., Kidd, W. S. F., & Steinhardt, C. (1988). Geometry and style of post-obduction thrusting in a Paleozoic orogen: The Taconic frontal thrust system. *The Journal of Geology*, *96*(2), 163–180. https://doi.org/10.1086/629207

Brandes, C., & Tanner, D. C. (2014). Fault-Related folding: A review of kinematic models and their application. *Earth-Science Reviews*, *138*, 352–370. https://doi.org/10.1016/j.earscirev.2014.06.008

Breuer, D., & Spohn, T. (2003). Early plate tectonics versus single-plate tectonics on Mars: Evidence from magnetic field history and crust evolution. *Journal of Geophysical Research*, *108*(E7). https://doi.org/10.1029/2002JE001999

Byrne, P. K., van Wyk de Vries, B., Murray, J. B., & Troll, V. R. (2012). A volcanotectonic survey of ascraeus mons, Mars. *Journal of Geophysical Research*, *117*(E1). https://doi.org/10.1029/2011JE003825

Chester, J. S., Logan, J. M., & Spang, J. H. (1991). Influence of layering and boundary conditions on fault-bend and fault-propagation folding. *Geological Society of America Bulletin*, *103*(8), 1059–1072. https://doi.org/10.1130/0016-7606(1991)103<1059:IOLABC>2.3.CO;2

Cole, H. M., & Andrews-Hanna, J. C. (2017). The anatomy of a wrinkle ridge revealed in the wall of Melas Chasma, Mars. *Journal of Geophysical Research: Planets*, *122*(5), 889–900. https://doi.org/10.1002/2017JE005274

Comer, R. P., Solomon, S. C., & Head, J. W. (1985). Mars: Thickness of the lithosphere from the tectonic response to volcanic loads. *Reviews of Geophysics*, *23*(1), 61–92. https://doi.org/10.1029/RG023i001p00061

Connors, C. D., Hughes, A. N., & Ball, S. M. (2021). Forward kinematic modeling of fault-bend folding. *Journal of Structural Geology*, *143*, 104252. https://doi.org/10.1016/j.jsg.2020.104252

Cowie, P. A., & Scholz, C. H. (1992). Physical explanation for the displacement-length relationship of faults using a post-yield fracture mechanics model. *Journal of Structural Geology*, *14*(10), 1133–1148. https://doi.org/10.1016/0191-8141(92)90065-5

Crane, K. (2020). Structural interpretation of thrust fault-related landforms on Mercury using Earth analogue fault models. *Geomorphology*, *369*, 107366. https://doi.org/10.1016/j.geomorph.2020.107366

Crane, K. T., & Klimczak, C. (2019a). Tectonic patterns of shortening landforms in Mercury's northern smooth plains. *Icarus*, *317*, 66–80. https://doi.org/10.1016/j.icarus.2018.05.034

Crane, K. T., & Klimczak, C. (2019b). *A 3-D structural model of the saddle mountains, Yakima Fold province, Washington, USA: Implications for late tertiary tectonic evolution of the columbia river flood basalt province*, (Vol. 766, pp. 1–13). Tectonophysics. https://doi.org/10.1016/j.tecto.2019.05.015

Crawley, M. J. (2015). *Statistics: An introduction using R*. John Wiley and Sons.

Egea-Gonzalez, I., Jiménez-Díaz, A., Parro, L. M., López, V., Williams, J. P., & Ruiz, J. (2017). Thrust fault modeling and Late-Noachian lithospheric structure of the Circum-Hellas region, Mars. *Icarus*, *288*, 53–68. https://doi.org/10.1016/j.icarus.2017.01.028

Egea-González, I., Ruiz, J., Fernández, C., Williams, J. P., Márquez, Á., & Lara, L. M. (2012). Depth of faulting and ancient heat flows in the Kuiper region of Mercury from lobate scarp topography. *Planetary and Space Science*, *60*(1), 193–198. https://doi.org/10.1016/j.pss.2011.08.003

Fergason, R. L., Hare, T. M., & Laura, J. (2018). HRSC and MOLA blended digital elevation model at 200m v2. In *Astrogeology PDS annex*. U.S. Geological Survey. https://doi.org/10.1029/2000JE001426/abstract

Gauthier, T. D. (2001). Detecting trends using Spearman's rank correlation coefficient. *Environmental Forensics*, *2*(4), 359–362. https://doi.org/10.1006/enfo.2001.0061

Golombek, M. P., Anderson, F. S., & Zuber, M. T. (2001). Martian wrinkle ridge topography: Evidence for subsurface faults from MOLA. *Journal of Geophysical Research*, *106*(E10), 23811–23821. https://doi.org/10.1029/2000JE001308

Golombek, M. P., & Phillips, R. J. (2010). Mars tectonics. *Planetary Tectonics*, *11*, 183–232. https://doi.org/10.1017/cbo9780511691645.006

Golombek, M. P., Plescia, J. B., & Franklin, B. J. (1991). Faulting and folding in the formation of planetary wrinkle ridges. In *Lunar and planetary science conference proceedings* (Vol. 21, pp. 679–693).

Grott, M., Hauber, E., Werner, S. C., Kronberg, P., & Neukum, G. (2007). Mechanical modeling of thrust faults in the Thaumasia region, Mars, and implications for the Noachian heat flux. *Icarus*, *186*(2), 517–526. https://doi.org/10.1016/j.icarus.2006.10.001

Gudmundsson, A., & Brenner, S. L. (2004). How mechanical layering affects local stresses, unrests, and eruptions of volcanoes. *Geophysical Research Letters Solid Earth*, *31*(16), L16606. https://doi.org/10.1029/2004GL020083

Hawman, R. B., Prosser, C. L., & Clippard, J. E. (2000). Shallow seismic reflection profiling over the Brevard zone, South Carolina. *Geophysics*, *65*(5), 1388–1401. https://doi.org/10.1190/1.1444829

Hayes, G. P., Wald, D. J., & Johnson, R. L. (2012). Slab1.0: A three-dimensional model of global subduction zone geometries. *Journal of Geophysical Research*, *117*(B1), B01302. https://doi.org/10.1029/2011JB008524

Heron, P. J., Pysklywec, R. N., Stephenson, R., & Van Hunen, J. (2019). Deformation driven by deep and distant structures: Influence of a mantle lithosphere suture in the Ouachita orogeny, southeastern United States. *Geology*, *47*(2), 147–150. https://doi.org/10.1130/G45690.1

Herrero-Gil, A., Egea-González, I., Ruiz, J., & Romeo, I. (2019). Structural modeling of lobate scarps in the NW margin of Argyre impact basin, Mars. *Icarus*, *319*, 367–380. https://doi.org/10.1016/j.icarus.2018.09.027

Herrero-Gil, A., Ruiz, J., & Romeo, I. (2020). 3D modeling of planetary lobate scarps: The case of Ogygis Rupes, Mars. *Earth and Planetary Science Letters*, *532*, 116004. https://doi.org/10.1016/j.epsl.2019.116004

Hopper, E., Fischer, K. M., Rondenay, S., Hawman, R. B., & Wagner, L. S. (2016). Imaging crustal structure beneath the southern Appalachians with wavefield migration. *Geophysical Research Letters*, *43*(23), 12–054. https://doi.org/10.1002/2016GL071005

Hughes, A. N., Benesh, N. P., & Shaw, J. H. (2014). Factors that control the development of fault-bend versus fault-propagation folds: Insights from mechanical models based on the Discrete Element Method (DEM). *Journal of Structural Geology*, *68*, 121–141. https://doi.org/10.1016/j.jsg.2014.09.009

Hughes, A. N., & Shaw, J. H. (2014). Fault displacement-distance relationships as indicators of contractional fault-related folding style. *AAPG Bulletin*, *98*(2), 227–251. https://doi.org/10.1306/05311312006

Jaeger, J. C., Cook, N. G., & Zimmerman, R. (2009). *Fundamentals of rock mechanics*. John Wiley and Sons.

Karagoz, O., Kenkmann, T., & Wulf, G. (2022). Insights into the subsurface structure of wrinkle ridges on Mars. *Earth and Planetary Science Letters*, *595*, 117759. https://doi.org/10.1016/j.epsl.2022.117759

Kaspar Arbenz, J. (2008). Structural framework of the Ouachita mountains in stratigraphic and structural evolution of the Ouachita mountains and arkoma basin. In N. H. Suneson (Ed.), *Southeastern Oklahoma and west-central Arkansas: Applications to petroleum exploration: 2024 field symposium*. Oklahoma Geological Survey.

Kelsey, H. M., Ladinsky, T. C., Staisch, L., Sherrod, B. L., Blakely, R. J., Pratt, T. L., et al. (2017). The story of a Yakima fold and how it informs late Neogene and Quaternary Backarc deformation in the Cascadia Subduction Zone, Manastash anticline, Washington, USA. *Tectonics*, *36*(10), 2085–2107. https://doi.org/10.1002/2017TC004558

Khan, A., Ceylan, S., van Driel, M., Giardini, D., Lognonné, P., Samuel, H., et al. (2021). Upper mantle structure of Mars from InSight seismic data. *Science*, *373*(6553), 434–438. https://doi.org/10.1126/science.abf2966

Klimczak, C., Kling, C. L., & Byrne, P. K. (2018). Topographic expressions of large thrust faults on Mars. *Journal of Geophysical Research: Planets*, *123*(8), 1973–1995. https://doi.org/10.1029/2017JE005448

Klimczak, C., Watters, T. R., Ernst, C. M., Freed, A. M., Byrne, P. K., Solomon, S. C., et al. (2012). Deformation associated with ghost craters and basins in volcanic smooth plains on Mercury: Strain analysis and implications for plains evolution. *Journal of Geophysical Research*, *117*(E12). https://doi.org/10.1029/2012JE004119

Korteniemi, J., Walsh, L. S., & Hughes, S. S. (2015). Wrinkle ridge. *Encyclopedia of planetary landforms*, 2324–2331. https://doi.org/10.1007/978-1-4614-3134-3_572

Kovarovic, K., Aiello, L. C., Cardini, A., & Lockwood, C. A. (2011). Discriminant function analyses in archaeology: Are classification rates too good to be true? Journal of archaeological science. *Journal of Archaeological Science*, *38*(11), 3006–3018. https://doi.org/10.1016/j.jas.2011.06.028

Kreslavsky, M. A., & Basilevsky, A. T. (1998). Morphometry of wrinkle ridges on Venus: Comparison with other planets. *Journal of Geophysical Research*, *103*(E5), 11103–11111. https://doi.org/10.1029/98JE00360

Laubscher, H. P. (1985). Large-scale, thin-skinned thrusting in the southern Alps: Kinematic models. *Geological Society of America Bulletin*, *96*(6), 710–718. https://doi.org/10.1130/0016-7606(1985)96<710:LTTITS>2.0.CO;2

Lay, T., Ye, L., Kanamori, H., & Satake, K. (2018). Constraining the dip of shallow, shallowly dipping thrust events using long-period love wave radiation patterns: Applications to the 25 October 2010 Mentawai, Indonesia, and 4 May 2018 Hawaii Island earthquakes. *Geophysical Research Letters*, *45*(19), 10–342. https://doi.org/10.1029/2018GL080042

Leverington, D. W., & Maxwell, T. A. (2004). An igneous origin for features of a candidate crater-lake system in western Memnonia, Mars. *Journal of Geophysical Research*, *109*(E6). https://doi.org/10.1029/2004JE002237

Lin, J., & Stein, R. S. (2004). Stress triggering in thrust and subduction earthquakes and stress interaction between the southern San Andreas and nearby thrust and strike-slip faults. *Journal of Geophysical Research*, *109*(B2). https://doi.org/10.1029/2003JB002607

Malin, M. C., BellIII, J. F., Cantor, B. A., Caplinger, M. A., Calvin, W. M., Clancy, R. T., et al. (2007). Context camera investigation on board the Mars reconnaissance orbiter. *Journal of Geophysical Research*, *112*(E5). https://doi.org/10.1029/2006JE002808

Mangold, N., Allemand, P., & Thomas, P. G. (1998). Wrinkle ridges of Mars: Structural analysis and evidence for shallow deformation controlled by ice-rich décollements. *Planetary and Space Science*, *46*(4), 345–356. https://doi.org/10.1016/S0032-0633(97)00195-5

McCullough, L. R., Crane, K., Loveless, S. R., & Klimczak, C. (2023). Morphological and structural characterization of shortening landforms on Mars datasets [Dataset]. *Zenodo*. https://doi.org/10.5281/zenodo.8322706

Medwedeff, D. A., & Suppe, J. (1997). Multibend fault-bend folding. *Journal of Structural Geology*, *19*(3–4), 279–292. https://doi.org/10.1016/S0191-8141(97)83026-X

Mitra, S. (1990). Fault-Propagation folds: Geometry, kinematic evolution, and hydrocarbon traps (1). *AAPG Bulletin*, *74*(6), 921–945. https://doi.org/10.1306/0C9B23CB-1710-11D7-8645000102C1865D

Mitra, S. (2002). Structural models of faulted detachment folds. *AAPG Bulletin*, *86*(9), 1673–1694. https://doi.org/10.1306/61EEDD3C-173E-11D7-8645000102C1865D

Montgomery, D. R., Som, S. M., Jackson, M. P., Schreiber, B. C., Gillespie, A. R., & Adams, J. B. (2009). Continental-scale salt tectonics on Mars and the origin of Valles Marineris and associated outflow channels. *Geological Society of America Bulletin*, *121*(1–2), 117–133. https://doi.org/10.1130/B26307.1

Mueller, K., & Golombek, M. (2004). Compressional structures on Mars. *Annual Review of Earth and Planetary Sciences*, *32*, 435–464. https://doi.org/10.1029/2002JE001974

Mueller, K., Vidal, A., Robbins, S., Golombek, M., & West, C. (2014). Fault and fold growth of the Amenthes uplift: Implications for Late Noachian crustal rheology and heat flow on Mars. *Earth and Planetary Science Letters*, *408*, 100–109. https://doi.org/10.1016/j.epsl.2014.09.047

Nahm, A. L., & Schultz, R. A. (2011). Magnitude of global contraction on Mars from analysis of surface faults: Implications for Martian thermal history. *Icarus*, *211*(1), 389–400. https://doi.org/10.1016/j.icarus.2010.11.003

Nimmo, F., & Stevenson, D. J. (2000). Influence of early plate tectonics on the thermal evolution and magnetic field of Mars. *Journal of Geophysical Research*, *105*(E5), 11969–11979. https://doi.org/10.1029/1999JE001216

Nimmo, F., & Watters, T. R. (2004). Depth of faulting on Mercury: Implications for heat flux and crustal and effective elastic thickness. *Geophysical Research Letters*, *31*(2). https://doi.org/10.1029/2003GL018847

Okubo, C. H., & Schultz, R. A. (2003). Thrust fault vergence directions on Mars: A foundation for investigating global-scale tharsis-driven tectonics. *Geophysical Research Letters*, *30*(22). https://doi.org/10.1029/2003GL018664

Okubo, C. H., & Schultz, R. A. (2004). Mechanical stratigraphy in the western equatorial region of Mars based on thrust fault–related fold topography and implications for near-surface volatile reservoirs. *Geological Society of America Bulletin*, *116*(5–6), 594–605. https://doi.org/10.1130/B25361.1

Phillips, R. J. (1992). Tectonic evolution of Mars (No. NASA-CR-194714).

Plescia, J. B. (1991). Wrinkle ridges in Lunae Planum Mars: Implications for shortening and strain. *Geophysical Research Letters*, *18*(5), 913–916. https://doi.org/10.1029/91GL01070

Ramsay, J. G. (1969). The measurement of strain and displacement in orogenic belts. *Geological Society, London, Special Publications*, *3*(1), 43–79. https://doi.org/10.1144/GSL.SP.1969.003.01.04

Rich, J. (2023). Limits of tectonic reactivation on Mars using Earth analogue analysis and numerical modeling. *Theses and Dissertations*, *5783*.

Robinson, D. M., DeCelles, P. G., & Copeland, P. (2006). Tectonic evolution of the Himalayan thrust belt in western Nepal: Implications for channel flow models. *Geological Society of America Bulletin*, *118*(7–8), 865–885. https://doi.org/10.1130/B25911.1

Ruj, T., & Kawai, K. (2021). A global investigation of wrinkle ridge formation events; implications towards the thermal evolution of Mars. *Icarus*, *369*, 114625. https://doi.org/10.1016/j.icarus.2021.114625

Ruj, T., Komatsu, G., Pondrelli, M., Di Pietro, I., & Pozzobon, R. (2018). Morphometric analysis of a Hesperian aged Martian lobate scarp using high-resolution data. *Journal of Structural Geology*, *113*, 1–9. https://doi.org/10.1016/j.jsg.2018.04.018

Sak, P. B., McQuarrie, N., Oliver, B. P., Lavdovsky, N., & Jackson, M. S. (2012). Unraveling the central Appalachian fold-thrust belt, Pennsylvania: The power of sequentially restored balanced cross sections for a blind fold-thrust belt. *Geosphere*, *8*(3), 685–702. https://doi.org/10.1130/GES00676.1

Schultz, P. H. (1976). Floor-fractured lunar craters. *The Moon*, *15*(3–4), 241–273. https://doi.org/10.1007/BF00562240

Schultz, R. A. (2000). Localization of bedding plane slip and backthrust faults above blind thrust faults: Keys to wrinkle ridge structure. *Journal of Geophysical Research*, *105*(E5), 12035–12052. https://doi.org/10.1029/1999JE001212

Schultz, R. A., Hauber, E., Kattenhorn, S. A., Okubo, C. H., & Watters, T. R. (2010). Interpretation and analysis of planetary structures. *Journal of Structural Geology*, *32*(6), 855–875. https://doi.org/10.1016/j.jsg.2009.09.005

Schultz, R. A., Okubo, C. H., & Wilkins, S. J. (2006). Displacement-length scaling relations for faults on the terrestrial planets. *Journal of Structural Geology*, *28*(12), 2182–2193. https://doi.org/10.1016/j.jsg.2006.03.034

Schultz, R. A., & Watters, T. R. (2001). Forward mechanical modeling of the Amenthes Rupes thrust fault on Mars. *Geophysical Research Letters*, *28*(24), 4659–4662. https://doi.org/10.1029/2001GL013468

Searle, M. P., Law, R. D., & Jessup, M. J. (2006). Crustal structure, restoration and evolution of the greater Himalaya in Nepal-South Tibet: Implications for channel flow and ductile extrusion of the middle crust. *Geological Society, London, Special Publications*, *268*(1), 355–378. https://doi.org/10.1144/gsl.sp.2006.268.01.17

Shaw, J. H., Connors, C., & Suppe, J. (2005). Seismic interpretation of contractional fault-related folds: An AAPG seismic atlas. *American Association of Petroleum Geologists*, *53*. https://doi.org/10.1306/St531003

Strom, R. G., Trask, N. J., & Guest, J. E. (1975). Tectonism and volcanism on Mercury. *Journal of Geophysical Research*, *80*(17), 2478–2507. https://doi.org/10.1029/JB080i017p02478

Suppe, J. (1983). Geometry and kinematics of fault-bend folding. *American Journal of Science*, *283*(7), 684–721. https://doi.org/10.2475/ajs.283.7.684

Suppe, J., & Medwedeff, D. A. (1990). Geometry and kinematics of fault-propagation folding.

Tanaka, K. L., Golombek, M. P., & Banerdt, W. B. (1991). Reconciliation of stress and structural histories of the Tharsis region of Mars. *Journal of Geophysical Research*, *96*(E1), 15617–15633. https://doi.org/10.1029/91JE01194

Tenzer, R., Eshagh, M., & Jin, S. (2015). Martian sub-crustal stress from gravity and topographic models. *Earth and Planetary Science Letters*, *425*, 84–92. https://doi.org/10.1016/j.epsl.2015.05.049

Toda, S., Stein, R. S., Sevilgen, V., & Lin, J. (2019). Coulomb 3.3 graphic-rich deformation and stress-change software for earthquake, tectonic, and volcano research and teaching— User guide. *U.S. Geological Survey*.

Watters, T., & Nimmo, F. (2010). *Planetary tectonics*. Cambridge University Press.

Watters, T. R. (1988). Wrinkle ridge assemblages on the terrestrial planets. *Journal of Geophysical Research*, *93*(B9), 10236–10254. https://doi.org/10.1029/JB093iB09p10236

Watters, T. R. (1991). Origin of periodically spaced wrinkle ridges on the Tharsis Plateau of Mars. *Journal of Geophysical Research*, *96*(E1), 15599–15616. https://doi.org/10.1029/91JE01402

Watters, T. R. (1992). System of tectonic features common to Earth, Mars, and Venus. *Geology*, *20*(7), 609–612. https://doi.org/10.1130/00917613(1992)020<0609:SOTFCT>2.3.CO;2

Watters, T. R. (1993). Compressional tectonism on Mars. *Journal of Geophysical Research*, *98*(E9), 17049–17060. https://doi.org/10.1029/93JE01138

Watters, T. R. (2004). Elastic dislocation modeling of wrinkle ridges on Mars. *Icarus*, *171*(2), 284–294. https://doi.org/10.1016/j.icarus.2004.05.024

Watters, T. R. (2021). A case for limited global contraction of Mercury. *Communications Earth & Environment*, *2*(1), 9. https://doi.org/10.1038/s43247-020-00076-5

Watters, T. R., & Robinson, M. S. (1999). Lobate scarps and the Martian crustal dichotomy. *Journal of Geophysical Research*, *104*(E8), 18981–18990. https://doi.org/10.1029/1998JE001007

Williams, N. R., Watters, T. R., Pritchard, M. E., Banks, M. E., & BellIII, J. F. (2013). Fault dislocation modeled structure of lobate scarps from Lunar Reconnaissance Orbiter Camera digital terrain models. *Journal of Geophysical Research: Planets*, *118*(2), 224–233. https://doi.org/10.1002/jgre.20051

Yue, Z., Michael, G. G., Di, K., & Liu, J. (2017). Global survey of lunar wrinkle ridge formation times. *Earth and Planetary Science Letters*, *477*, 14–20. https://doi.org/10.1016/j.epsl.2017.07.048

Zoback, M. D. (2007). *Reservoir geomechanics*. Cambridge University Press. https://doi.org/10.1017/CBO9780511586477

Zoback, M. L. (1992). Stress field constraints on intraplate seismicity in eastern North America. *Journal of Geophysical Research*, *97*(B8), 11761–11782. https://doi.org/10.1029/92JB00221

Zuber, M. T., Montési, L. G., Farmer, G. T., HauckII, S. A., Ritzer, J. A., Phillips, R. J., et al. (2010). Accommodation of lithospheric shortening on Mercury from altimetric profiles of ridges and lobate scarps measured during MESSENGER flybys 1 and 2. *Icarus*, *209*(1), 247–255. https://doi.org/10.1016/j.icarus.2010.02.026